Lebedev Scheme for Ultrasound Simulation in Composites

Francisco Hernando Quintanilla[a], Cara A.C. Leckey[a,*]

[a]*NASA Langley Research Center, Hampton, VA, USA*

Abstract

The growing use of composite materials for aerospace applications has resulted in a need for quantitative nondestructive evaluation (NDE) methods appropriate for characterizing damage in composite components. NDE simulation tools, such as ultrasound models, can aid in enabling optimized inspection methods and establishing confidence in inspection capabilities. In this paper a mathematical approach using the Lebedev Finite Difference (LFD) method is presented for ultrasonic wave simulation in composites. Boundary condition equations for implementing stress-free boundaries (necessary for simulation of NDE scenarios) are also presented. Quantitative comparisons between LFD guided wave ultrasound simulation results, experimental guided wave data, and dispsersion curves are described. Additionally, stability tests are performed to establish the LFD code behavior in the presence of stress-free boundaries and low-symmetry anisotropy. Results show that LFD is an appropriate approach for simulating ultrasound in anisotropic composite materials and that the method is stable in the presence of low-symmetry anisotropy and stress-free boundaries. Studies presented in this paper include guided wave simulation in hexagonal, monoclinic, triclinic and layered composite laminates.

Keywords: Guided wave, Lebedev method, Simulation, Composite

1. Introduction

The growing use of composite materials for aerospace applications has resulted in a need for quantitative nondestructive evaluation (NDE) methods appropriate for characterizing damage in composite components. With the recent development of advanced manufacturing techniques, such as automated fiber placement, composite structures with geometries more complex than flat or low radius of curvature cylindrical shapes are becoming more common. Ultrasound based NDE methods are commonly used in the aerospace field, but ultrasonic wave behavior can be complicated by the presence of material anisotropy, complex geometries, and complex geometry defect types. Common defects occurring in aerospace composites include delaminations, porosity, and microcracking. Physics based simulation tools that model ultrasonic energy propagation can aid in the development of optimized inspection methods and in the interpretation of NDE data. Both the complex geometries of composite aerospace components (e.g., highly curved parts, stiffeners, and joints) and the complex geometries of composite defects lead to a need for fully three-dimensional (3D) NDE simulation tools.

3D ultrasound modeling for composite structures poses the challenge of accounting for variations in geometry and the associated forms of the stiffness matrix c_{ijkl}. The elastic behavior of a typical unidirectional carbon fiber reinforced polymer (CFRP) prepreg material can be accurately modeled as a hexagonal (transversely isotropic) medium. In order to model the fiber direction of a complex part, rotations must be applied to the hexagonal material to follow a prescribed curved path in 3D space. As a consequence, the stiffness matrix of the hexagonal material will undergo analogous rotations resulting in a transformed stiffness matrix with the structure of a monoclinic or triclinic material (in the most general case).Thus, the increasing use of composites with complex geometries makes it essential that NDE simulation tools can accurately and reliably model media of the most general anisotropy: triclinic.

In the field of NDE, researchers primarily use two approaches for modeling elastic wave propagation: Finite Differences (FD) and Finite Element (FE) algorithms. The FE approach is used by several commercial software packages, such as COMSOL and ABAQUS. However, very large FE simulations can be extremely computationally expensive due to the required inversion of the mass matrix. FD schemes do not suffer this inversion drawback since they can be coded to implement simple algebraic equations. Creating custom ultrasound simulation code based on a FD mathematical foundation has several benefits, including: complete control over the mathematics performed, ability to computationally optimize the code for memory efficiency and speed, ability to adapt the code to the latest computational hardware (with a smaller lag-time compared to commercial tools), ability to create parallelized code to lever-

age computing cluster and/or many-integrated-core (MIC) architectures [1]. One popular FD algorithm is the Elastodynamic Finite Integration Technique (EFIT) [2], which was proposed for NDE applications by Marklein et al [3]. This numerical scheme has also been used by Schubert et al. [4], Halkjaer [5] and, more recently, by Leckey et al. [6] for NDE ultrasound modeling in transversely isotropic composites. Leckey et. al implemented a custom EFIT code for composites in order to leverage high performance computing parallelization approaches that allow for large sized simulation domains through improved computational efficiency [1, 6]. Prior work by Wheeler et al. compared the accuracy and computational requirements of custom EFIT code versus FE commercial software packages for simple laminate problems [7].

The EFIT algorithm falls into the broader family of FD schemes known as explicit time-domain staggered grid methods. Staggered grid FD algorithms have been used for many decades in the geophysics community to model elastic wave propagation in anisotropic media, see Virieux [8, 9] for example. Initial investigations of geophysical problems mostly involved isotropic and transversely isotropic media for which the straggered grid scheme proposed by Virieux performed accurately and reliably in a wide variety of settings. The need to model media with a lower degree of symmetry such as monoclinic and triclinic anisotropy revealed that the staggered grid scheme proposed by Virieux suffered from an inherent numerical instability arising from the averaging of the off-block-diagonal elastic constants. This instability was investigated and quantified by Igel et. al. [10]. Igel showed that the instability was not related to the Von Neumann stability criterion but to the required interpolation and averaging of elastic constants and stresses at grid points where they are not defined.

Using the anisotropic EFIT scheme discussed in [5, 6], local instabilities have been observed at the locations of stress-free boundaries when modeling monoclinic and triclinic plates. Figure 1 shows an example of the instabilities observed for the monoclinic case discussed in section 3.3. Testing of the anisotropic EFIT code showed that the instability onset time is much smaller for discontinuous excitation signals compared to that for smooth excitation signals. As described by Strikwerda, this behavior confirms the source of the stability is likely related to the numerical scheme [11]. In accordance with the aforementioned study by Igel et. al, it is noted that no instabilities have been observed with EFIT for hexagonal (e.g., transversely isotropic) material cases [6].

The contribution of this article is to present a second order 3D Lebedev FD (LFD) scheme as an stable alternative to the second order EFIT scheme for FD based modeling of ultrasound in generally anisotropic structures for NDE applications. The LFD scheme is shown to perform stably for general anisotropic media (triclinic), thus

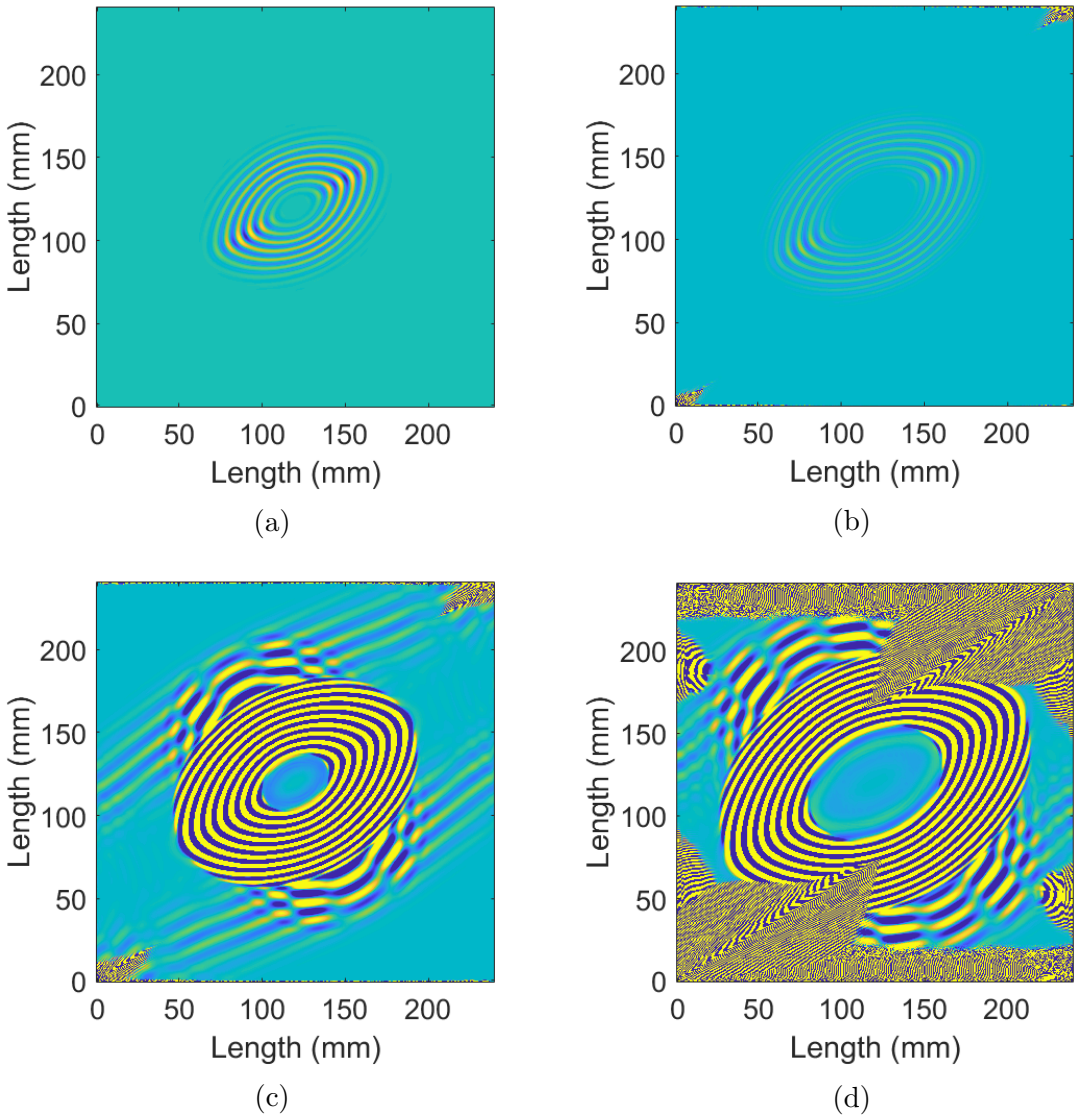

Figure 1: Wavefield images showing snapshots in time of EFIT simulation results for a monoclinic CFRP laminate (v_z at the plate surface is shown) : (a) A_0 mode propagation at a time before numerical instabilities begin, (b) A_0 mode propagation at a time after numerical instabilities have started at the simulation edges/corners (visible as large amplitude features emerging from corners), (c) image at the same point in time shown in (b) but with the colorscale saturated to show S_0, SH_0, and A_0 modes, (d) a later point in time showing numerical instabilities overtaking the simulation space.

making the method an option for NDE ultrasound modeling of complex geometry composites and for laminates containing rotated transversely isotropic (i.e., monoclinic) plies. Furthermore, NDE applications often involve reflection of ultrasound from stress-free boundaries (e.g., component edges, defects that behave as stress-free boundaries such as open delaminations). Examples of wave scattering from stress-free boundaries for generally anisotropic media have not been reported previously in the literature (to the knowledge of the authors). In this work the authors show that appropriate stress-free boundary conditions can be implemented in the LFD scheme. The scheme is validated by comparison to experimental data and dispersion curves. The LFD method belongs to the family of staggered grid FD schemes and was originally developed by Lebedev [12, 13]. The method was recently proposed for modeling elastic wave propagation in anisotropic media by Lisitsa et. al. [14, 15].

One of the main features of the LFD scheme is that all elastic constants and density values are stored at the node locations where they are used to perform computations. This grid setup is in stark contrast to other staggered grid schemes, such as EFIT or that of Virieux, which store physical constants at the cell centers and use interpolated values elsewhere. This important difference is what makes the LFD scheme stable when modeling monoclinic and triclinic materials. Improved performance (stability and higher accuracy for the same density of nodes, [14]) is achieved at the cost of using four interpenetrating staggered grids. This more complex grid (compared to methods such as EFIT) leads to a denser distribution of nodes and hence a more computationally demanding code in terms of memory requirements and number of operations for a given spatial and time step. Nevertheless, the higher computational cost can be greatly mitigated by employing parallel algorithms which run on many-core and cluster computers.

Another alternative approach, commonly used in geophysics, is the Rotated Staggered Grid (RSG) FD scheme developed by Saenger et. al [16]. RSG is reported to satisfactorily handle generally anisotropic media as shown in [16], its main feature being that it computes the derivatives along the diagonals of the elementary cell. As with the LFD approach, examples of scattering from stress-free boundaries for generally anisotropic media have not been reported (to the knowledge of the authors). A comparative study between RSG and LFD approaches was carried out by Lisitsa et. al. [14]. The study demonstrated that, for prescribed result accuracy, the RSG requires a denser grid than the LFD, leading to even higher computational demand. For a thorough review of 3D elastic wave computational methods, including FE approaches, FD methods, Pseudo-spectral method [17], and the more computationally complex Spectral Element Method (SEM) [18, 19], see [9].

As stated above, this paper outlines the LFD approach and the stress-free bound-

ary conditions required for NDE simulation of ultrasonic waves in composite materials. The results presented here establish the suitability of the LFD scheme for simulating ultrasound in low symmetry anisotropic media containing stress-free boundaries. While the LFD method is a general elastodynamic modeling approach that allows for simulation of bulk and guided wave ultrasound, the validation studies presented here are based on guided wave behavior in CFRP laminates. Section 2 presents the mathematics of the LFD scheme for composites including stress-free boundary conditions. Section 3 describes the guided waves comparisons that were performed between simulation, experiment, and dispersion curves. Examples of LFD stability for anisotropic composites with stress-free boundaries is also presented. Section 4 summarizes the results and discusses future work.

2. 3D Lebedev Finite Difference Scheme for Composites

2.1. The Grid

The main distinguishing feature of the Lebedev Finite Difference (LFD) scheme is the approach used for construction of the FD grid from the elementary cell and the associated storage of the physical parameters. The global grid is composed of four staggered grids [15], two of which correspond to the velocity field and and two for the stress field of the body. A diagram of the LFD grid can be seen in figure 2 where diamonds mark the locations of the velocity grid and solid circles correspond to the stress grid. In contrast to other staggered grid schemes, relevant physical parameters are stored at all grid points in order to avoid the need for averaging at locations where an operation is performed but no parameters are available. For the LFD scheme, material density is stored at the velocity grid points and the stiffness matrix values are stored at stress grid points.

Each grid point is determined by three *non-negative* integral indices (i, j, k) corresponding to the three discrete coordinates (x, y, z). To match the usual indexing of programming languages, the grids are defined as follows: $\Gamma_\sigma = \{(i,j,k)|i+j+k = 2m; m \in \mathbb{N}\cup\{0\}\}$ for the stresses, and $\Gamma_u = \{(i,j,k)|i+j+k = 2m+1; m \in \mathbb{N}\cup\{0\}\}$ for velocities. Other indexing choices are possible which are entirely equivalent to that used in this paper, see [14].

2.2. 3D LFD Equations

The usual notational convention for FD schemes will be adopted: $[f]^n_{ijk} \equiv f(t^n, x_i, y_j, z_k)$. The derivatives in time and space are approximated by second order stencils. For the derivative in the x direction at time level n:

$$D_x[f]^n_{ijk} = \frac{f^n_{i+1jk} - f^n_{i-1jk}}{\Delta_x} \tag{1}$$

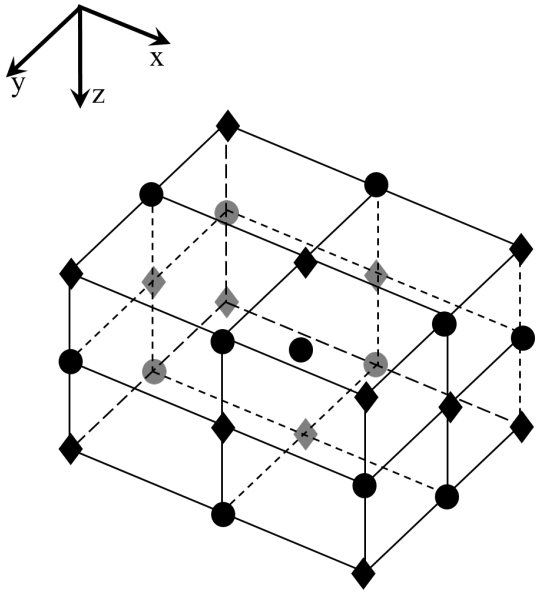

Figure 2: A single grid cell in the LFD scheme, where diamonds represent velocity locations and circles show the location of stresses.

and equivalently for the other two derivatives. For the time derivative at the point (ijk) we have a similar expression:

$$D_t[f]^n_{ijk} = \frac{f^{n+1/2}_{ijk} - f^{n-1/2}_{ijk}}{\Delta_t} \tag{2}$$

The LFD equations are readily derived using the above expressions from the well-known wave equations for anisotropic elastic media, see for instance [20, 14]. For the components of the velocity field u_γ with $\gamma = x, y, z$ one has:

$$\begin{gathered}[\rho]_{ijk} D_t[u_\gamma]^{n+1/2}_{ijk} = \textstyle\sum_{\alpha=x,y,z} D_\alpha[\sigma_{\gamma\alpha}]^{n+1/2}_{ijk} \\ (i,j,k) \in \Gamma_u\end{gathered} \tag{3}$$

For the expression of the stresses σ_I in terms of the strains ϵ_J the reduced index notation, $I, J = 1, ..., 6$ is employed, see [20]

$$D_t[\sigma_I]^n_{ijk} = \sum_{J=1}^{6} c_{IJ}[\epsilon_J]^n_{ijk} \qquad (i,j,k) \in \Gamma_\sigma \tag{4}$$

where the strains are given by the following, see [20, 14]:

$$[\epsilon_J]^n_{ijk} = \begin{pmatrix} D_x[u_x]^n_{ijk} \\ D_y[u_y]^n_{ijk} \\ D_z[u_z]^n_{ijk} \\ D_y[u_z]^n_{ijk} + D_z[u_y]^n_{ijk} \\ D_z[u_x]^n_{ijk} + D_x[u_z]^n_{ijk} \\ D_x[u_y]^n_{ijk} + D_y[u_x]^n_{ijk} \end{pmatrix} \tag{5}$$

2.3. Boundary Conditions

In this section the implementation of stress-free boundary conditions for generally anisotropic media is described. The main challenge when explicitly implementing these boundary conditions is to do so without the requirement of computing the normal strains to the boundary under consideration (which would involve taking normal derivatives). Thus, the goal is to express the non-zero stress components in terms of only tangential strains, which can be evaluated on the boundaries. In order to do this, the boundary conditions are used to solve for the normal strains in terms of the tangential strains at the boundary.

For faces with $z = z_f.$ one begins with the usual stress-free boundary conditions:

$$\sigma_{zz}|_{z=z_f.} = \sigma_{zx}|_{z=z_f.} = \sigma_{zy}|_{z=z_f.} = 0 \tag{6}$$

Expressing these three conditions in matrix form makes it clear how to proceed, from equation (4):

$$\begin{pmatrix} 0 \\ 0 \\ 0 \end{pmatrix} = \begin{pmatrix} c_{13} & c_{23} & c_{33} & c_{34} & c_{35} & c_{36} \\ c_{14} & c_{24} & c_{34} & c_{44} & c_{45} & c_{46} \\ c_{15} & c_{25} & c_{35} & c_{45} & c_{55} & c_{56} \end{pmatrix} \begin{pmatrix} \epsilon^n_{xx} \\ \epsilon^n_{yy} \\ \epsilon^n_{zz} \\ \epsilon^n_{yz} \\ f\epsilon^n_{xz} \\ \epsilon^n_{xy} \end{pmatrix}_{z=z_f.} \tag{7}$$

the tangential components of the strain $\epsilon^n_{xx}, \epsilon^n_{yy}$ and ϵ^n_{xy} can be evaluated. By splitting the above equation one obtains:

$$-\begin{pmatrix} c_{13} & c_{23} & c_{36} \\ c_{14} & c_{24} & c_{46} \\ c_{15} & c_{25} & c_{56} \end{pmatrix} \begin{pmatrix} \epsilon^n_{xx} \\ \epsilon^n_{yy} \\ \epsilon^n_{xy} \end{pmatrix}_{z=z_f.} = \begin{pmatrix} c_{33} & c_{34} & c_{35} \\ c_{34} & c_{44} & c_{45} \\ c_{35} & c_{45} & c_{55} \end{pmatrix} \begin{pmatrix} \epsilon^n_{zz} \\ \epsilon^n_{yz} \\ \epsilon^n_{xz} \end{pmatrix}_{z=z_f.} \tag{8}$$

more succinctly:

$$-\mathbb{A}\epsilon^n_{\parallel} = \mathbb{B}\epsilon^n_{\perp} \tag{9}$$

where $\mathbb{A}$ and $\mathbb{B}$ represent the matrices listed in (7), $\epsilon^n_{\parallel}$ and $\epsilon^n_{\perp}$ are the tangential and normal to boundary strain components respectively. Solving for $\epsilon^n_{\perp}$ in terms of $\epsilon^n_{\parallel}$:

$$\epsilon^n_{\perp} = -\mathbb{B}^{-1}\mathbb{A}\epsilon^n_{\parallel} = \mathbb{E}\epsilon^n_{\parallel} \tag{10}$$

The non-zero stress components at the boundary $z = z_f.$ can be written as:

$$\begin{pmatrix} \sigma^n_{xx} \\ \sigma^n_{yy} \\ \sigma^n_{xy} \end{pmatrix} = \begin{pmatrix} c_{11} & c_{12} & c_{16} \\ c_{12} & c_{22} & c_{26} \\ c_{16} & c_{26} & c_{66} \end{pmatrix} \epsilon^n_{\parallel} + \begin{pmatrix} c_{13} & c_{14} & c_{15} \\ c_{23} & c_{24} & c_{25} \\ c_{36} & c_{46} & c_{56} \end{pmatrix} \epsilon^n_{\perp} \tag{11}$$

More compactly to allow for future manipulations, one can write:

$$\epsilon^n_{\parallel} = \mathbb{F}_{\parallel}\epsilon^n_{\parallel} + \mathbb{F}_{\perp}\epsilon^n_{\perp} \tag{12}$$

Substituting equation (10) into equation (12) one obtains the final expression for the non-zero tangential stresses at the boundaries in terms of the tangential strains that can be evaluated at the boundaries $z = z_f.$:

$$\sigma^n_{\parallel} = (\mathbb{F}_{\parallel} + \mathbb{F}_{\perp}\mathbb{E})\epsilon^n_{\parallel} \tag{13}$$

For edges parallel to the z axes one begins with the usual stress-free boundary conditions:

$$\begin{aligned} \sigma_{xx}|_{x,y=z_f} = \sigma_{yy}|_{x,y=z_f} = 0 \\ \sigma_{xz}|_{x,y=z_f} = \sigma_{yz}|_{x,y=z_f} = \sigma_{xy}|_{x,y=z_f} = 0 \end{aligned} \tag{14}$$

This approach yields a larger analogue of equation (7):

$$\begin{pmatrix} 0 \\ 0 \\ 0 \\ 0 \\ 0 \end{pmatrix} = \begin{pmatrix} c_{11} & c_{12} & c_{13} & c_{14} & c_{15} & c_{16} \\ c_{12} & c_{22} & c_{23} & c_{24} & c_{25} & c_{26} \\ c_{14} & c_{24} & c_{34} & c_{44} & c_{45} & c_{46} \\ c_{15} & c_{25} & c_{35} & c_{45} & c_{55} & c_{56} \\ c_{16} & c_{26} & c_{36} & c_{46} & c_{56} & c_{66} \end{pmatrix} \begin{pmatrix} \epsilon^n_{xx} \\ \epsilon^n_{yy} \\ \epsilon^n_{zz} \\ \epsilon^n_{yz} \\ \epsilon^n_{xz} \\ \epsilon^n_{xy} \end{pmatrix}_{z=z_f.} \tag{15}$$

Splitting the equation into tangential and perpendicular strain components one has:

$$\begin{aligned} \begin{pmatrix} c_{11} & c_{12} & c_{14} & c_{15} & c_{16} \\ c_{12} & c_{22} & c_{24} & c_{25} & c_{26} \\ c_{14} & c_{24} & c_{44} & c_{45} & c_{46} \\ c_{15} & c_{25} & c_{45} & c_{55} & c_{56} \\ c_{16} & c_{26} & c_{46} & c_{56} & c_{66} \end{pmatrix} \begin{pmatrix} \epsilon^n_{xx} \\ \epsilon^n_{yy} \\ \epsilon^n_{yz} \\ \epsilon^n_{xz} \\ \epsilon^n_{xy} \end{pmatrix}_{z=z_f} = \\ - \begin{pmatrix} c_{13} \\ c_{23} \\ c_{34} \\ c_{35} \\ c_{36} \end{pmatrix} \begin{pmatrix} \epsilon^n_{zz} \end{pmatrix}_{z=z_f.} \end{aligned} \tag{16}$$

equivalent to:

$$\mathbb{G}\epsilon^n_{\perp} = -\mathbb{H}\epsilon^n_{zz} \tag{17}$$

Solving for $\epsilon^n_{\perp}$ in terms of ϵ^n_{zz} :

$$\epsilon^n_{\perp} = -\mathbb{G}^{-1}\mathbb{H}\epsilon^n_{\parallel} = \mathbb{K}\epsilon^n_{zz} \tag{18}$$

where $\mathbb{K}$ is a column vector. The non-zero stress component along a z-edge is σ^n_{zz} and is given by:

$$\sigma^n_{zz} = c_{33}\epsilon^n_{zz} + (c_{13}c_{23}c_{34}c_{35}c_{36})\epsilon^n_{\perp} \tag{19}$$

Upon substitution of equation (17) in equation (18):

$$\sigma_{zz}^{n} = [c_{33} + (c_{13}c_{23}c_{34}c_{35}c_{36})\mathbb{K}]\epsilon_{zz}^{n} \tag{20}$$

the equation above is the stress-free boundary condition to be imposed for any edge parallel to the z edge.

The procedure for faces and edges with different orientations is analogous to the approach just described, and will yield similar expressions which will be omitted here for brevity.

3. Validation Comparisons and Stability Check

Quantitative validation comparisons of LFD results against experiment are performed using wavenumber domain kx-ky plots. Since the experimental setup described in section 3.1 only allows for measurement of out-of-plane v_z motion, wavenumber comparisons between simulation and experiment are performed for the A_0 anti-symmetric mode, which has a much higher out-of-plane amplitude compared to the in-plane dominant S_0 and SH_0 modes. In order to check the simulated S_0 and SH_0 modes, comparisons are performed against dispersion curve values.

3.1. Experimental Setup

Three test panels made of IM7/8552 CFRP (an aerospace grade composite material) were fabricated at NASA Langley Research Center. Table 1 lists elastic material properties for a single ply of IM7/8552 based on values reported in the scientific literature [22, 23, 24]. The three different laminate specimens were fabricated with layups: 1) 0.952 mm thick eight ply unidirectional plate (transversely isotropic case in section 3.2), 2) 1.44 mm thick eight ply monoclinic plate with fibers in all plies at a 30-degree angle (section 3.3), 3) 0.96 mm thick eight ply quasi-isotropic plate with layup [0/45/-45/90]s (section 3.5). The quasi-isotropic case is used to check the LFD method's ability to model laminae with multiple ply layers of different material orientations using the corresponding transformed stiffness matrices.

For all specimens guided ultrasonic waves were excited in the specimens using a GE Inspection Technologies Gamma Series (TCG-999) 0.5 MHz contact piezo-electric transducer (PZT). In all cases the transducer was driven by a 200 kHz 3-cycle Hann-windowed sine wave. All simulation cases used this same signal for the excitation source.

Experimental wavefield data was collected using a Polytec OFV-505 LDV connected to an OFV-5000 controller with a 1 MHz high-frequency cutoff. The LDV

Table 1: IM7/8552 material properties (for a single ply, with E1 in the fiber direction)

Property	IM7/8552
ρ (kg/m^3)	1570
E_1 (GPa)	171.4
E_2 (GPa)	9.08
E_3 (GPa)	9.08
G_{12} (GPa)	5.29
G_{13} (GPa)	5.29
G_{23} (GPa)	2.80
ν_{12}	0.320
ν_{13}	0.320
ν_{23}	0.5

is attached to a two-axis scanning system to acquire out-of-plane velocity measurements on a pre-defined x-y Cartesian grid. The LDV is set up to collect data for the CFRP laminate surface opposite to the PZT actuator, see Rogge and Leckey [21]. The out-of-plane velocity signals recorded by the LDV were digitized at a sampling rate of 20 MHz.

3.2. Transversely Isotropic (Hexagonal) Plates

In this and all subsequent simulations a cubic grid is used and the spatial step size, Δx, is set small enough to resolve the shortest wavelength occurring in the simulation.The recommended upper bound for Δx reported in the literature is $\lambda_{min}/8$ [4]. For all simulation studies presented here the order of magnitude of the spatial step size is $\Delta x = \lambda_{min}/40$. Additionally, in order to ensure computational stability and convergence, the time step must satisfy the Courant-Friedrich-Levy (CFL) condition, which for cubic grids is $\Delta t \leq \Delta x/(c_{max}\sqrt{3})$ (where c_{max} is the maximum wavespeed in the simulation). The hexagonal simulation case was implemented with Δx=0.095 mm, Δt=4.72 ns and an overall simulation size of 3000 x 3000 x 10 grid cells (10 in the thickness direction, $\hat{z}$).

Time domain wavefield plots for the transversely isotropic case are shown in Figure 3. The plots show v_z at the specimen surface at a single point in time for both the simulated and experimental wavefields. The colormap is chosen to display the A_0 mode propagation. It is noted that in both cases the plots are for a subset of the entire simulation domain and experimental scan space, hence there is no wave scattering shown in the figures. As shown in the figure, the general shape of

the two wavefields is similar. For a more quantitative comparison, a 3D Fourier Transform is applied to the space-time domain wavefield data in order to transform the data into wavenumber-frequency domain (x-wavenumber (k_x) vs. y-wavenumber (k_x) vs. frequency) [6]. The frequency slice corresponding to the center frequency of excitation (200 kHz) is then selected and is plotted in Figure 4. Note that the dark circle in the center of the experimental result is created due to the finite size of the excitation source (transducer), for more details see prior work by Leckey et. al. [6].

Plotting the data in terms of k_x vs. k_y allows for a quantitative comparison of the resulting guided wave mode wavenumbers for all propagation directions. As shown in figure 4, the wavenumber plots show a dark ring which corresponds to the amplitude of the corresponding guided wave mode in each direction. By selecting the wavenumber value occuring at the center of the band in a specific direction (i.e., a single pixel location within the wavenumber ring), a single value for wavenumber can be estimated for a given direction. The pixel resolution is determined by the bin size of the Fourier Transform. Table 2 shows the A_0 wavenumber values for k_x with $k_y = 0$ (along the 0-degree fiber direction) and k_y with $k_x = 0$ (90-degree direction perpendicular to the fibers). The resolution reported in the table corresponds to half of the pixel resolution of the k_x vs. k_y plot. Since the experimental data only corresponds to the out-of-plane motion (i.e., primarily corresponding to the out-of-plane mode, A_0), Table 3 shows comparisons between simulation and dispersion curve wavenumber values for the dominantly in-plane modes, S_0 and SH_0 [25].

It is noted that the wavenumber domain analysis is particularly well-suited for a quantitative comparison to experiment in cases where the various guided wave modes are clearly distinguishable in the k_x vs. k_y plots. In the hexagonal case presented here, the SH_0 mode wavenumber along the 90-degree direction from LFD was difficult to clearly determine due to the overlapping of the S_0 mode (see figure 4). Table 3 therefore lists two potential SH_0 wavenumbers. The larger value is based on the v_x plot which appears to show a sharply curved rise of the SH_0 wavenumber band around the 90-degree direction (vertical direction in the plot). The smaller wavenumber value listed in the table for SH_0 is based on the v_y plot which also contains the overlapping S_0 mode, but does not show as much of an indication of a sharp curve around 90-degrees. The SH_0 wavenumber listed in the table for LFD in the 90-degree direction is thus considered to be less certain.

3.3. Monoclinic Laminates

Laminates containing monoclinic plies are common for aerospace applications. The case of a monoclinic ply orientation results from rotating a unidirectional ply to an angle different from multiples of 90-degrees. As shown in the matrix below, the re-

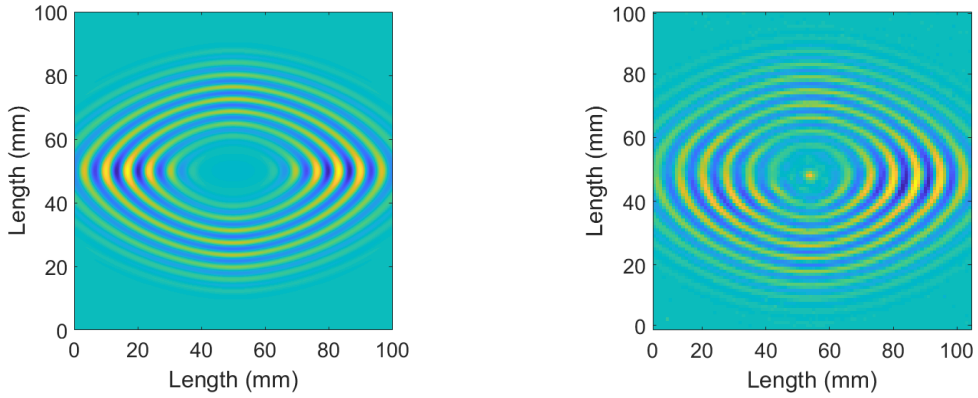

(a) Simulation, v_z (b) Experiment, v_z

Figure 3: Wavefield plots for the transversely isotropic plate case, showing out-of-plane velocity, v_z, at a single point in time for simulated and measured wavefields.

Table 2: Transversely isotropic case A_0 wavenumber comparisons.

Method	0° k $(1/m)$		90° k $(1/m)$	
	Value	Resolution	Value	Resolution
Experiment, A_0	128.9	± 3.90	228.55	± 3.90
LFD, A_0	146.14	± 2.56	260.30	± 2.56
Dispersion Curves, A_0	141.74	−−	252.64	−−

Table 3: Transversely isotropic case S_0 and SH_0 wavenumber comparisons.

Method	0° k $(1/m)$		90° k $(1/m)$	
	Value	Resolution	Value	Resolution
LFD, S_0	20.51	± 2.56	83.35	± 2.56
Dispersion Curves, S_0	19.09	−−	83.14	−−
LFD, SH_0	110.28	± 2.56	87.18 or 107.7*	± 2.56
Dispersion Curves, SH_0	109.70	−−	108.94	−−

*see text in section 3.2

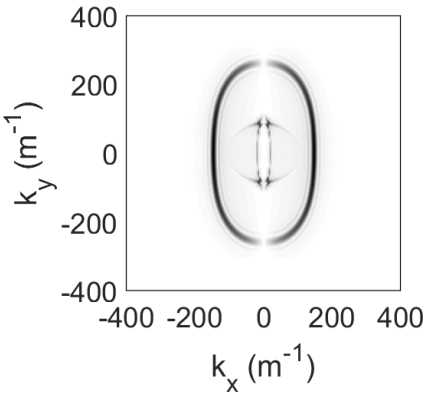

(a) Simulation, v_x wavenumbers

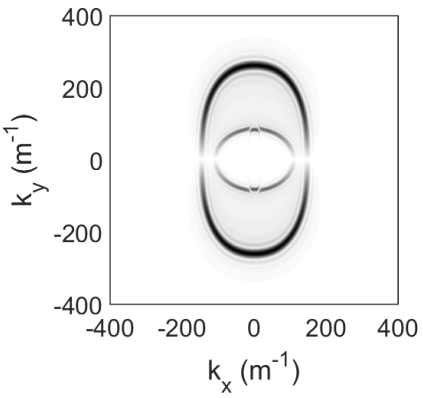

(b) Simulation, v_y wavenumbers

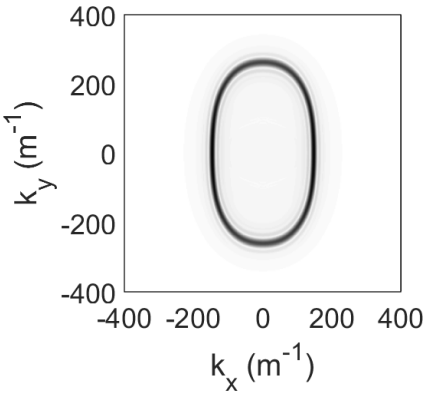

(c) Simulation, v_z wavenumbers

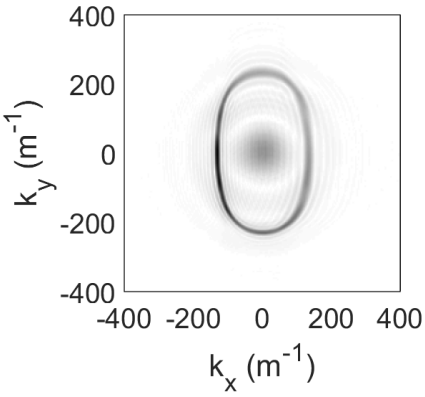

(d) Experiment, v_z wavenumbers

Figure 4: Wavenumber plots at the center excitation frequency for the transversely isotropic plate case, showing (k_x, k_y) for simulated and measured wavefields. Simulation results are shown for v_x, v_y, v_z. Experimental results are shown for v_z

sulting stiffness matrix contains additional off-diagonal non-zero elements compared to the transversely isotropic case.

$$c_{ijkl} = \begin{pmatrix} c_{11} & c_{12} & c_{13} & 0 & 0 & c_{16} \\ c_{12} & c_{22} & c_{23} & 0 & 0 & c_{26} \\ c_{13} & c_{23} & c_{33} & 0 & 0 & c_{36} \\ 0 & 0 & 0 & c_{44} & c_{45} & 0 \\ 0 & 0 & 0 & c_{45} & c_{55} & 0 \\ c_{16} & c_{26} & c_{36} & 0 & 0 & c_{66} \end{pmatrix} \tag{21}$$

The monoclinic case studied for validation corresponds to the eight ply experimental specimen with fibers in all layers running in the 30-degree direction, see the diagram in Figure 5. The monoclinic simulation was implemented with spatial step size Δx=0.08 mm and time step size Δt=3.97 ns. The simulation size of 3000 x 3000 x 18 grid cells thus corresponds to 240 mm x 240 mm x 1.44 mm.

Time domain wavefield plots for the monoclinic case are shown in Figure 6. The plots shows v_z at a single point in time at the specimen surface for both the simulated and experimental wavefields. The colormap is chosen to display the A_0 mode propagation. As in the transversely isotropic wavefield plots, Figure 6 plots are for a subset of the entire simulation domain and experimental scan space, hence there is no wave scattering shown in the figures. Again, it is observed that the general shape of the two wavefields is very similar.

Figure 7 shows simulation wavefield (v_z) snapshots for later points in time once the A_0 mode has scattered from plate edges. The LFD method is observed to be stable for scattering from stress-free boundaries in low-symmetry anisotropy cases (such as monoclinic). In fact, Figure 7(a) shows the LFD results for the same case and the same point in time as the EFIT results in Figure 1 which displayed unstable behavior.

The corresponding k_x vs. k_y plots for the center excitation frequency (200 kHz) are shown in Figure 8. Table 4 shows the A_0 wavenumber values for k_x at $k_y = 0$ (along the 0-degree fiber direction) and k_y at $k_x = 0$ (90-degree direction perpendicular to the fibers). Table 5 shows comparisons between simulation and dispersion curve wavenumber values for S_0 and SH_0 modes [25]. As discussed in section 3.2, the SH_0 wavenumber in the 90-degree direction is less certain due to the overlap of the S_0 mode.

3.3.1. Additional Rotations

Flat CFRP components require stiffness matrix rotations in a single plane (e.g., about the z-axis, see figure 5) in order to appropriately represent the ply level prop-

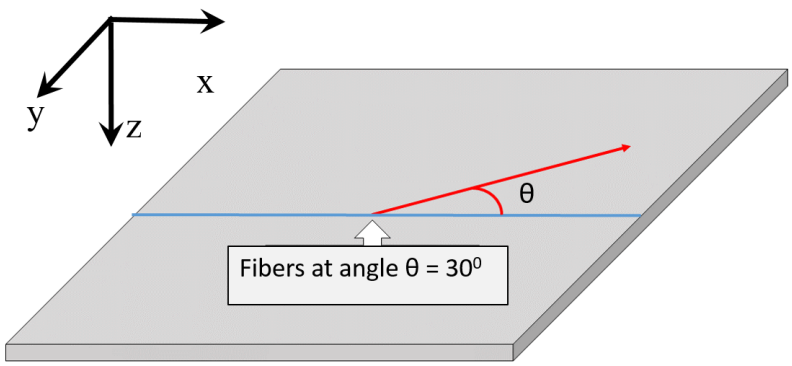

Figure 5: Monoclinic case with fibers in all plies running in the 30-degree direction.

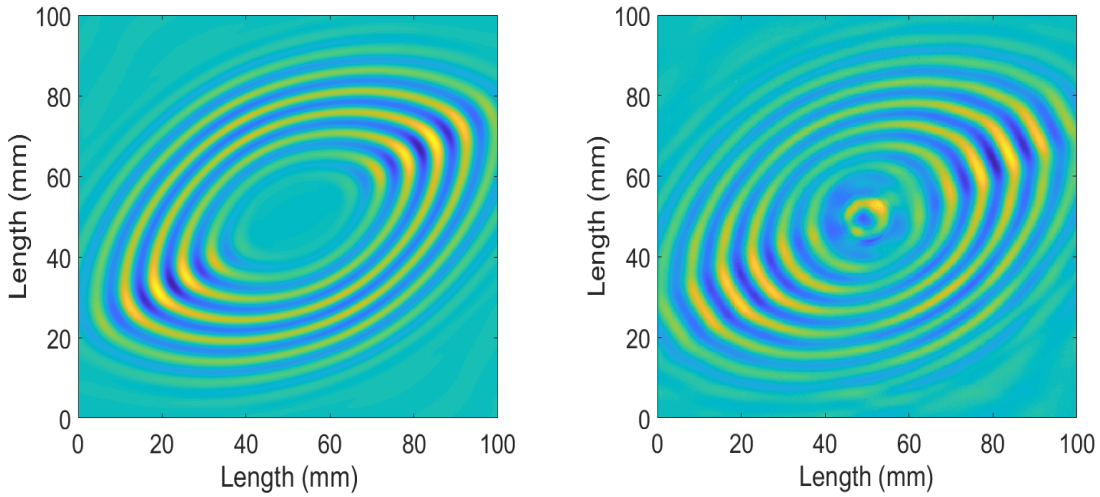

(a) Simulation, v_z (b) Experiment, v_z

Figure 6: Wavefield plots for the monoclinic plate case, showing out-of-plane velocity, v_z, at a single point in time for simulated and measured wavefields.

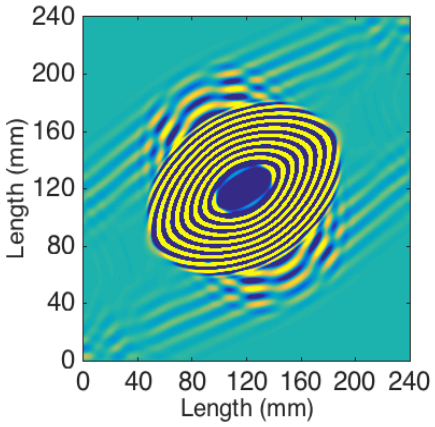

(a) Time, t_1 (colormap saturated).

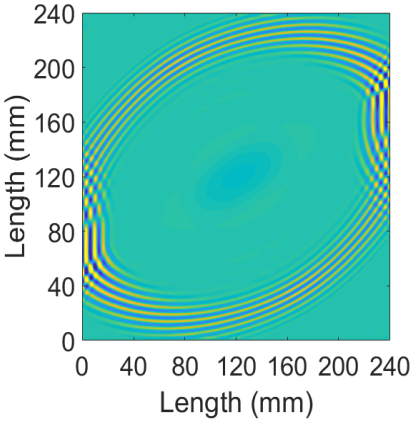

(b) Time, t_2

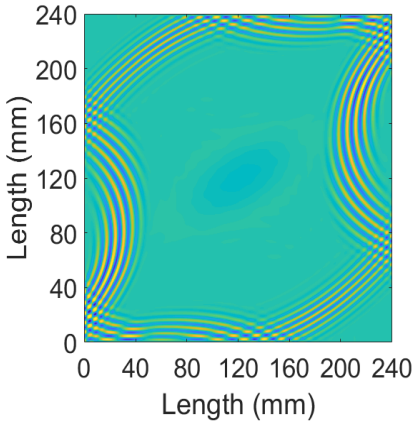

(c) Time, t_3

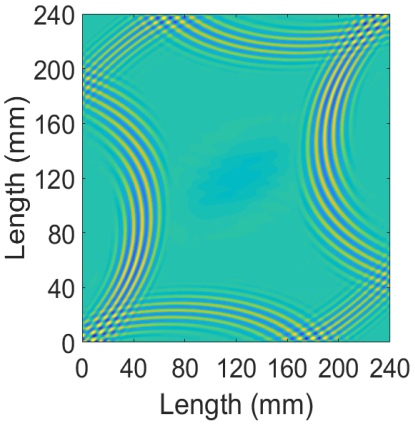

(d) Time, t_4

Figure 7: Wavefield plots of simulated v_z for the monoclinic case for snapshots in time showing edge scattering. Note that the colormap in (a) is saturated to show S_0 and SH_0 modes. The colormap in (b)-(d) is chosen to show A_0 mode scattering.

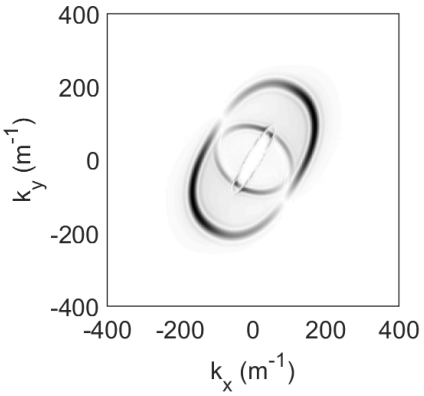

(a) Simulation, v_x wavenumbers

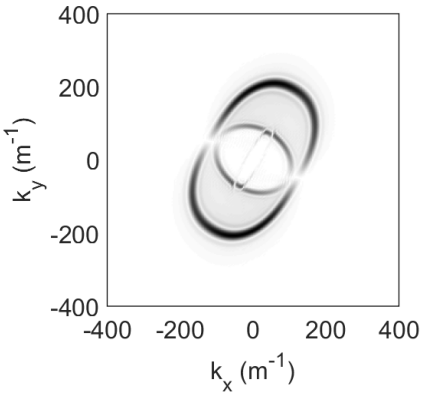

(b) Simulation, v_y wavenumbers

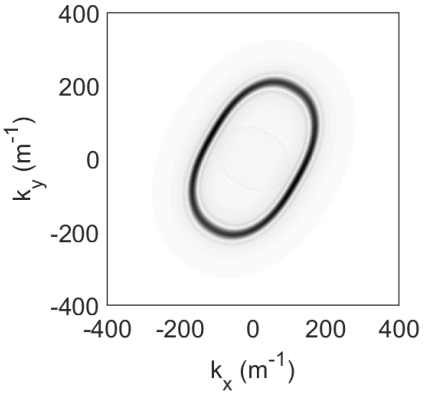

(c) Simulation, v_z wavenumbers

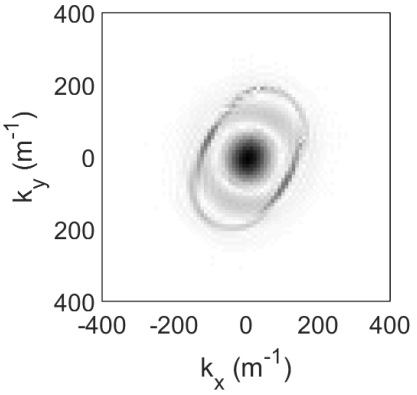

(d) Experiment, v_z wavenumbers

Figure 8: Wavenumber plots at the center excitation frequency for the monoclinic plate case, showing (k_x, k_y) for simulated and measured wavefields. Simulation results are shown for (a) v_x, (b) v_y, (c) v_z. Experimental results are shown in (d) for v_z.

Table 4: Monoclinic case A_0 wavenumber comparisons.

Method	$0°$ k $(1/m)$		$90°$ k $(1/m)$	
	Value	Resolution	Value	Resolution
Experiment, A_0	127.31	$\pm$ 9.80	222.88	$\pm$ 9.80
LFD, A_0	131.35	$\pm$ 3.00	225.58	$\pm$ 3.00
Dispersion Curves, A_0	130.09	$--$	218.71	$--$

Table 5: Monoclinic case S_0 and SH_0 wavenumber comparisons.

Method	$0°$ k $(1/m)$		$90°$ k $(1/m)$	
	Value	Resolution	Value	Resolution
LFD, S_0	22.21	$\pm$ 3.00	84.79	$\pm$ 3.00
Dispersion Curves, S_0	18.93	$--$	84.45	$--$
LFD, SH_0	106.59	$\pm$ 3.00	91.61	$\pm$ 3.00
Dispersion Curves, SH_0	109.69	$--$	108.96	$--$

erties due to the layup. The monoclinic case discussed thus far assumed a scenario where the geometry and ply rotation led to specific non-zero terms in the stiffness matrix. However, aerospace composite components often contain tightly curved regions, composite joints, and stiffeners (e.g., hat or T stiffeners) which are more complex than a simple plate-like geometry. These more complex geometries require additional rotations of the stiffness matrix to accurately represent the resulting material properties (for example, a rotation about both the z-axis and the x-axis). Such a rotation leads to additional non-zero terms in the stiffness matrix. The most general case of anisotropy, triclinic with all non-zero stiffness matrix terms, may be relevant for some complex geometry components.

In order check additional mathematical terms in the Lebedev equations (terms associated with other non-zero elements of the stiffness matrix), two additional rotation cases were simulated corresponding to the stiffness matrices shown below. These cases are the exact same as the monoclinic case in the prior seciton, but represent a rotation of the material into another plane (see figure 9). Since a triclinic composite specimen was unavailable for validation comparisons, these two additional rotated monoclinic cases along with the monoclinic case discussed in the prior session allow

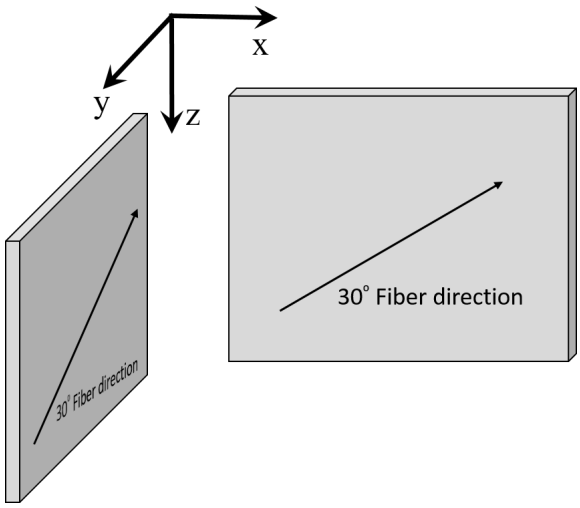

Figure 9: Diagram showing rotations corresponding to matrices (20) and (21).

for comparisons to experiment by iterative implementation of all possible terms in the stiffness matrix (and all corresponding mathematical terms in LFD). These two cases resulted in the same wavenumber values as the monoclinic case in the prior section, hence they will not be re-listed here (see Tables 4, 5).

For the case with a rotation about the x-axis the stiffness matrix is of the form:

$$c_{ijkl} = \begin{pmatrix} c_{11} & c_{12} & c_{13} & c_{14} & 0 & 0 \\ c_{12} & c_{22} & c_{23} & c_{24} & 0 & 0 \\ c_{13} & c_{23} & c_{33} & c_{34} & 0 & 0 \\ c_{14} & c_{24} & c_{34} & c_{44} & 0 & 0 \\ 0 & 0 & 0 & 0 & c_{55} & c_{56} \\ 0 & 0 & 0 & 0 & c_{56} & c_{66} \end{pmatrix} \tag{22}$$

For the case with a rotation about the y-axis the stiffness matrix is of the form:

$$c_{ijkl} = \begin{pmatrix} c_{11} & c_{12} & c_{13} & 0 & c_{15} & 0 \\ c_{12} & c_{22} & c_{23} & 0 & c_{25} & 0 \\ c_{13} & c_{23} & c_{33} & 0 & c_{35} & 0 \\ 0 & 0 & 0 & c_{44} & 0 & c_{46} \\ c_{15} & c_{25} & c_{35} & 0 & c_{55} & 0 \\ 0 & 0 & 0 & c_{46} & 0 & c_{66} \end{pmatrix} \tag{23}$$

Figure 10 shows a single snapshot in time of the simulation resulting from the

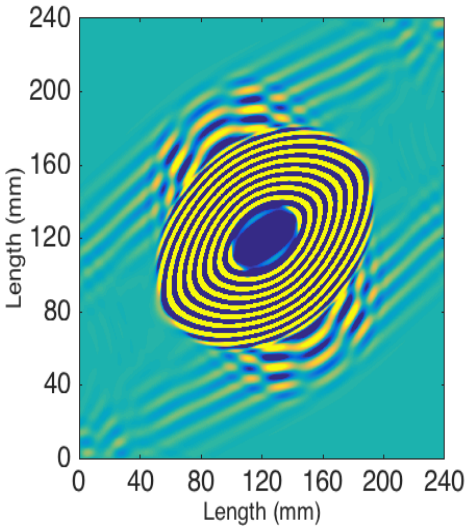

Figure 10: Wavefield plot of v_z for the stiffness matrix corresponding to (20). Compare to figure 7(a).

stiffness matrix in (20). As expected, the result appears identical the results in figure 7(a). This result is also identical to the wavefield resulting from the simulation using the stiffness matrix form in (21).

3.4. Triclinic Stability

Further testing was implemented to check the stability of a fully triclinic case. The stiffness matrix for the IM7/8552 material was rotated first by 30-degrees about the z-axis and then 45-degrees about the new y-axis. The specific rotation angles were chosen at random, with the overall goal of yielding a fully populated stiffness matrix. The resulting stiffness matrix is shown below (in units of GPa, and symmetric about the diagonal):

$$c_{ijkl} = \begin{pmatrix} 37.10 & 20.52 & 27.77 & -17.55 & -23.28 & 19.07 \\ & 24.05 & 20.52 & -13.10 & -14.35 & 13.10 \\ & & 37.10 & -19.07 & -23.28 & 17.55 \\ & & & 18.82 & 18.41 & -15.40 \\ & & & & 26.42 & -18.41 \\ & & & & & 18.82 \end{pmatrix} \tag{24}$$

Figure 11 shows wave scattering from stress free edge boundadries for this fully triclinic case. As shown in the figure, there are no instability issues observed for the

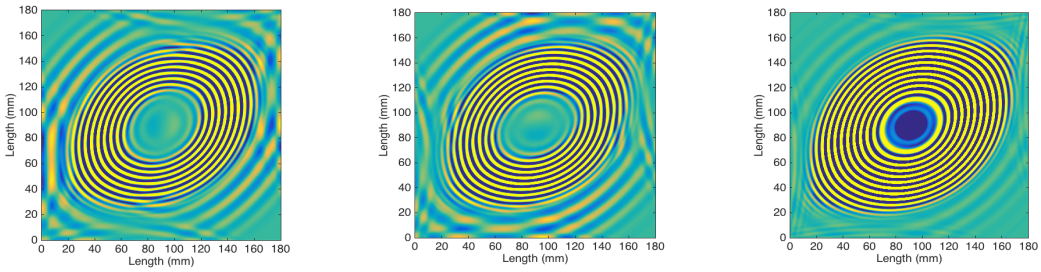

(a) Time t_1, v_x (b) Time t_1, v_y (c) Time t_1, v_z

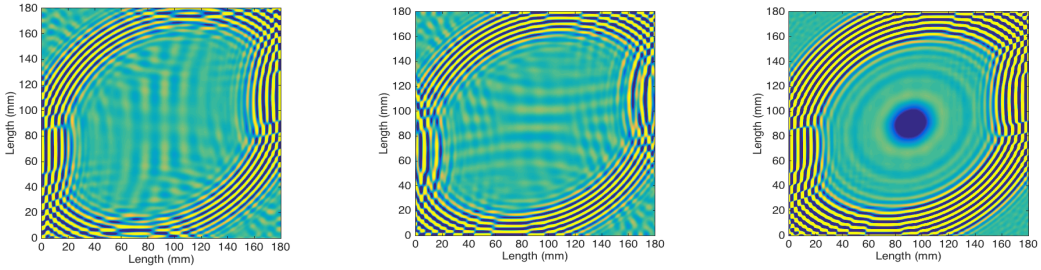

(d) Time t_2, v_x (e) Time t_2, v_y (f) Time t_2, v_z

Figure 11: Wavefield plots of v_x, v_y, and v_z for the simulated triclinic case for snapshots in time showing edge scattering. The stress-free boundary scattering shows numerically stable behavior.

LFD method.

3.5. Multi-Layered Laminates: Quasi-Isotropic Case

The final comparison performed for the initial benchmarking of the LFD approach is simulation of a multiple ply layer quasi-isotropic laminate. Guided waves in an eight ply [0/45/-45/90]s laminate, corresponding to the associated experimental specimen described in Section 3.1, were simulated.

The simulation spatial and time step sizes were set to Δx=0.06 mm and Δt=2.98 ns. The simulated laminate was 3000 x 3000 x 16 cells 3000 cells (16 cells in the z direction with 2 cells per ply).

For cases involving multiple materials or a single CFRP material with different ply layer orientations, no specific continuity conditions are imposed at the boundaries. The averaging of variables over neighbouring cells that is performed at each node suffices to take into account the physics at the interfaces. A detailed study on 2D interface performance of the LFD scheme, albeit in a geophysics setting, was reported by Lisitsa et. al. [27].

Time domain wavefield plots for the simulated quasi-isotropic case are shown in

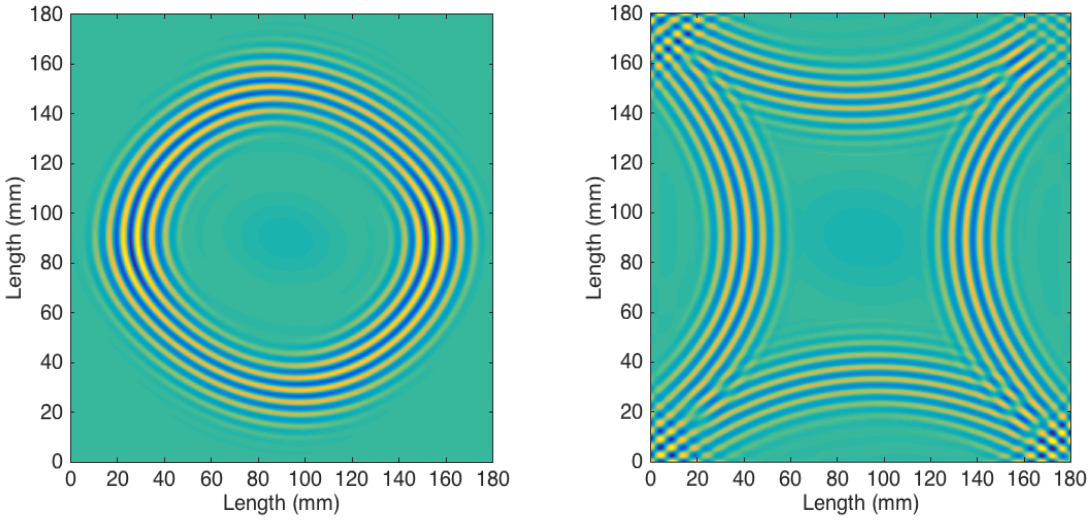

(a) Simulation, v_z (b) Simulation, v_z

Figure 12: Wavefield plots for the quasi-isotropic plate case, showing out-of-plane velocity from simulation, v_z, at two points in time. The figure on the right shows stability under stress-free boundary edge scattering.

Figure 12. The plots shows the simulated v_z wavefield on the plate surface at two points in time. The colormap is chosen to display the A_0 mode propagation. The second point in time shows scattering from the stress-free edge boundaries. The results demonstrate a successful implementation of simulation for a multi-layered composite. Furthermore, the LFD method again shows stable behavior in the presence of stress-free boundaries. The corresponding k_x vs. k_y plots for the center excitation frequency (200 kHz) are shown in Figure 13. Table 6 shows the A_0 wavenumber values for 0-degree and 90-degree directions.

Table 6: Quasi-isotropic check cases A_0 wavenumber comparisons.

Method	0° k $(1/m)$		90° k $(1/m)$	
	Value	Resolution	Value	Resolution
Experiment, A_0	156.23	$\pm$ 7.80	179.7	$\pm$ 7.80
LFD, A_0	164.80	$\pm$ 4.10	203.48	$\pm$ 4.10
Dispersion Curves A_0	165.70	$--$	200.40	$--$

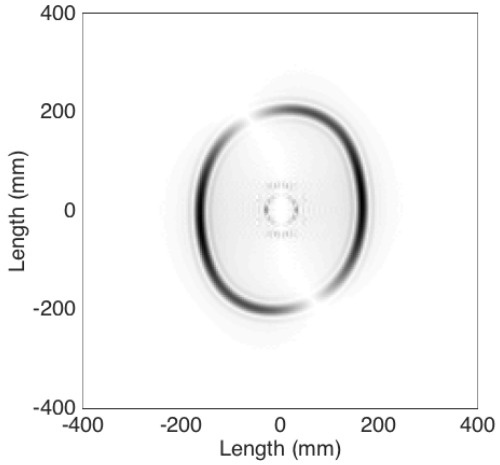

(a) Simulation, v_x wavenumbers

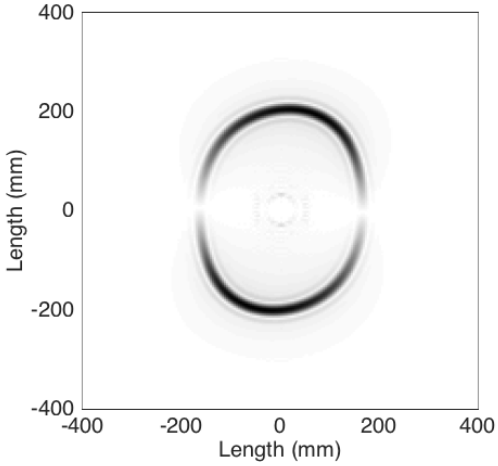

(b) Simulation, v_y wavenumbers

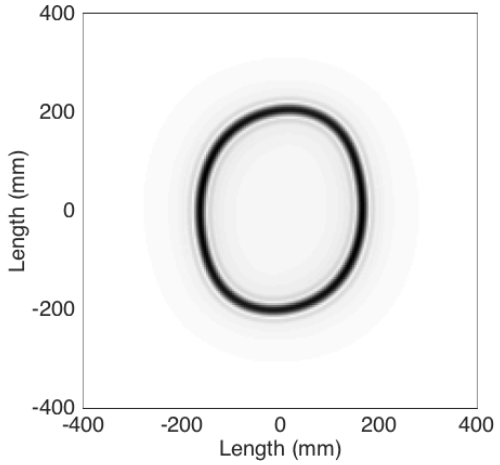

(c) Simulation, v_z wavenumbers

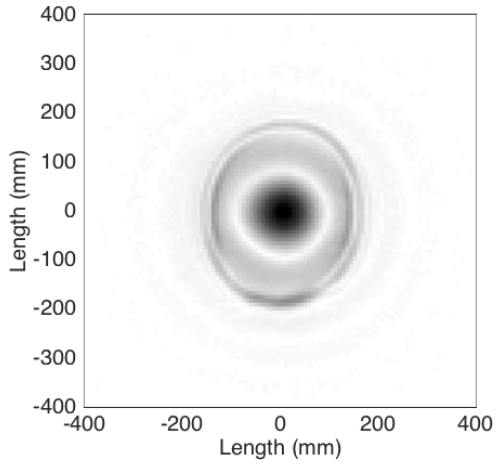

(d) Experiment, v_z wavenumbers

Figure 13: Wavenumber plots at the center excitation frequency for the quasi-isotropic plate case, showing (k_x, k_y) for simulated and measured wavefields. Simulation results are shown for v_x, v_y, v_z. Experimental results are shown for v_z

4. Conclusion

The results presented in this paper demonstrate that the LFD approach is appropriate for simulation of ultrasonic wave propagation in composites. LFD was successfully implemented for hexagonal, monoclinic, triclinic, and multi-layer laminates. The wavenumber results from the Lebedev method matched well with experiment and dispersion curves. As discussed in [6], some differences from experiment are expected due to uncertainty in the actual as-manufactured material properties of the composite specimens. The LFD wavenumbers were between 1 to 13 % different from experiment, and overall it is noted that experiment consistently led to lower wavenumbers than LFD simulation. This trend was not consistently observed when comparing LFD to dispersion curves (i.e., dispersion curves sometimes led to a larger value than LFD). Recall that LFD and dispersion curves are both based on the material properties in Table 1, which were taken from the literature. The observed trend in experimental wavenumbers may be a clue that there is indeed a consistent difference between the material properties in experiment versus simulation. Recent work by Reed et. al also points to this possibility [29].

Additionally, it was shown that LFD is stable for low-symmetry anisotropic media and in the presence of stress-free boundaries. Stability for low-symmetry anisotropic cases is critical for simulating ultrasonic NDE in complex geometry composites (geometries requiring multiple stiffness matrix rotations, such as hat-stiffeners and complex curvature parts). The observed stability in the presence of stress-free boundaries is also of key importantance for simulating NDE scenarios since they often involve ultrasonic wave scattering from part surfaces, edges, and corners. Furthermore, defects such as microcracking and delaminations can be simulated using stress-free boundaries [7, 28].

Future areas of work include optimization of the LFD code for more rapid simulations on MIC computing hardware. The initial code version used for the studies in this paper took multiple days to run a single simulation case on 30 CPU cores. Based on prior work with finite difference code optimization, it is expected that significant simulation speed increases can be achieved by optimizing the code parallelization and memory access patterns [1]. Future work will also entail the use of the LFD code to simulate ultrasound in complex geometry aerospace composites and adapting the code to include material based attenuation.

5. Acknowledgements

The authors thank NASA interns Christina Cole and Ashley Frank for assistance collecting experimental data. The authors also thank Dr. Vadim Lisitsa, Dr. Paul

Fromme, Dr. Frank Schubert, Prof. Jean Virieux, Prof. Dimitri Komatitsch, Prof. Romain Brossier, Prof. Heiner Igel, Dr. René Marklein and Prof. Erik Saenger for helpful discussions regarding the stability of FD approaches for anisotropic media.

[1] C. Leckey, J. Seebo, Guided wave energy trapping to detect hidden multilayer delamination damage, Rev Progr Quant Nondestr AIP Publishing, 1650 (2015) 1162–1169.

[2] F. Fellinger, K.J. Langenberg, Numerical techniques for elastic wave propagation and scattering, Proc IUTAM Sym (1990) 81–86.

[3] R. Marklein, The finite integration technique as a general tool to compute acoustic, electromagnetic, elastodynamic, and coupled wave fields, Rev Radio Sci: 1999-2002 URSI, edited by W. Stone, IEEE Press and John Wiley and Sons, New York, pp. 201–244 (2002).

[4] F. Schubert, A. Peiffer, B. Kohler, T. Sanderson, The elastodynamic finite integration technique for waves in cylindrical geometries, J Acoust Soc Am 104 (1998) 2604–2614.

[5] S. Halkjaer, Elastic wave propagation in anisotropic inhomogeneous materials, Ph.D. dissertation, Technical University of Denmark, Lyngby Denmark (available from `http://www2.imm.dtu.dk/documents/ftp/phdliste/phd74.abstract.html`, date last viewed: 5/17/2012) (2000).

[6] C. Leckey, M. Rogge, F.Parker, Guided waves in anisotropic and quasi-isotropic aerospace composites: Three dimensional simulation and experiment, Ultrasonics 54 (2014) 385–394.

[7] K. Wheeler, C. Leckey, V. Hafiychuk, P. Juarez, D. Timucin, S. Schuet, H. Hafiychuk, Benchmarking of computational models for NDE and SHM of composites, Proc Amer Soc Comp (2016) 2912.

[8] J. Virieux, P-SV wave propagation in heterogeneous media: Velocity-stress finite-difference method, Geophysics 51.4 (1986) 889–901.

[9] J. Virieux, H. Calandra, R. Plessix, A review of the spectral, pseudospectral, finitedifference and finiteelement modelling techniques for geophysical imaging, Geophysical Prospecting 59.5 (2011) 794–813.

[10] H. Igel, P. Mora, B. Riollet, Anisotropic wave propagation through finite-difference grids, Geophysics 60.4 (1995) 1203–1216.

[11] J. Strikwerda, Finite difference schemes and partial differential equations, Wadsworth Publ. Co., Belmont, CA (1989).

[12] V. Lebedev, Difference analogues of orthogonal decompositions, fundamental differential operators and certain boundary-value problems of mathematical physics I, USSR Comput Mathematics and Mathematical Phys 4.3 (1964) 69–92.

[13] V. Lebedev, Difference analogues of orthogonal decompositions, fundamental differential operators and certain boundary-value problems of mathematical physics II, USSR Comput Mathematics and Mathematical Phys 4.4 (1964) 649–659.

[14] V. Lisitsa, D. Vishnevskiy, Lebedev scheme for the numerical simulation of wave propagation in 3D anisotropic elasticity, Geophysical Prospecting 58.4 (2010) 619–635.

[15] V. Lisitsa, D. Vishnevskiy, On specific features of the Lebedev scheme in simulating elastic wave propagation in anisotropic media, Numerical Analysis and Applications 4.2 (2011) 125–135.

[16] E. Saenger, T. Bohlen, Finite-difference modeling of viscoelastic and anisotropic wave propagation using the rotated staggered grid, Geophysics 69.2 (2004) 583–591.

[17] J. Carcione, P. Wang, A Chebyshev collocation method for the wave equation in generalized coordinates, Comp. Fluid Dyn. J 2 (1993) 269–290.

[18] D. Komatitsch, R. Martin, An unsplit convolutional perfectly matched layer improved at grazing incidence for the seismic wave equation, Geophysics 72.5 (2007)SM155–SM167.

[19] D. Komatitsch, S. Tsuboi, J. Tromp, The spectralelement method in seismology, Seismic earth: Array analysis of broadband seismograms (2005): 205–227.

[20] B. Auld, Acoustic waves and fields in solids, New York: Wiley and Sons 1 (1973).

[21] M. Rogge, C. Leckey, Characterization of impact damage in composite laminates using guided wavefield imaging and local wavenumber domain analysis, Ultrasonics 53.7 (2013) 1217-1226.

[22] Hexcel Prepreg Datasheet 8552, `http://www.hexcel.com/user_area/content_media/raw/HexPly_8552_eu_DataSheet.pdf` Hexcel Corp (2016).

[23] P.P. Camanho, P. Maimi, C.G. Davila, Prediction of size effects in notched laminates using continuum damage mechanics, Compos Sci Technol 67 (2007) 2715–2727.

[24] A.S. Kaddour, M.J. Hinton, S. Li, P. Smith, Instructions to the contributors of the third world-wide failure exercise (WWFE-III): part A, (2008).

[25] B.N. Pavlakovic, M.J.S. Lowe Disperse: a general purpose program for creating dispersion curves, Rev Prog Quant Nondestr 16A (1997) 155–192.

[26] T.E. Michaels, J.E. Michaels, M. Ruzzenne Frequency-wavenumber domain analysis of guided wavefields, Ultrasonics (2011) 452–466.

[27] D. Vishnevskiy, V. Lisitsa, V. Tcheverda, G. Reshetova Numerical study of interface errors of finite-difference simulations of seismic waves, Geophys 79.4 (2014) 219–232.

[28] Z. Tian, L. Yu, C. Leckey Delamination detection and quantification on laminated composite structures with Lamb waves and wavenumber analysis, J Intell Mater Sys Struct 26.13 (2015): 1723-1738.

[29] H. Reed, C. Leckey, A. Dick, G. Harvey, J. Dobson A model based bayesian solution for characterization of complex damage scenarios in aerospace composite structures, Ultras, *under review*